

CHEMOUT: CHEMical complexity in star-forming regions of the OUTER Galaxy

III. Nitrogen isotopic ratios in the outer Galaxy

L. Colzi¹, D. Romano², F. Fontani³, V. M. Rivilla¹, L. Bizzocchi⁴, M. T. Beltrán³, P. Caselli⁵, D. Elia⁶, and L. Magrini³

¹ Centro de Astrobiología (CAB), CSIC-INTA, Ctra. de Ajalvir Km. 4, 28850, Torrejón de Ardoz, Madrid, Spain
e-mail: lcolzi@cab.inta-csic.es

² INAF, Osservatorio di Astrofisica e Scienza dello Spazio, Via Gobetti 93/3, 40129, Bologna, Italy

³ INAF-Osservatorio Astrofisico di Arcetri, Largo E. Fermi 5, I-50125, Florence, Italy

⁴ Department of Chemistry “Giacomo Ciamician”, University of Bologna, Via F. Selmi 2, Bologna, 40126, Italy

⁵ Centre for Astrochemical Studies, Max-Planck-Institute for Extraterrestrial Physics, Giessenbachstrasse 1, 85748 Garching, Germany

⁶ INAF - IAPS, via Fosso del Cavaliere, 100, I-00133 Roma, Italy

Accepted 16 September 2022. Received 29 July 2022

ABSTRACT

Context. Nitrogen isotopic ratios are a key tool for tracing Galactic stellar nucleosynthesis.

Aims. We present the first study of the $^{14}\text{N}/^{15}\text{N}$ abundance ratio in the outer regions of the Milky Way (namely, for galactocentric distances, R_{GC} , from 12 kpc up to 19 kpc), with the aim to study the stellar nucleosynthesis effects in the global Galactic trend.

Methods. We analysed IRAM 30m observations towards a sample of 35 sources in the context of the CHEMical complexity in star-forming regions of the OUTER Galaxy (CHEMOUT) project. We derived the $^{14}\text{N}/^{15}\text{N}$ ratios from HCN and HNC for 14 and 3 sources, respectively, using the $J = 1-0$ rotational transition of HN^{13}C , H^{15}NC , H^{13}CN , and HC^{15}N .

Results. The results found in the outer Galaxy have been combined with previous measurements obtained in the inner Galaxy. We find an overall linear decreasing $\text{H}^{13}\text{CN}/\text{HC}^{15}\text{N}$ ratio with increasing R_{GC} . This translates to a parabolic $^{14}\text{N}/^{15}\text{N}$ ratio with a peak at 11 kpc. Updated Galactic chemical evolution models have been taken into account and compared with the observations. The parabolic trend of the $^{14}\text{N}/^{15}\text{N}$ ratio with R_{GC} can be naturally explained (i) by a model that assumes novae as the main ^{15}N producers on long timescales (≥ 1 Gyr) and (ii) by updated stellar yields for low- and intermediate-mass stars.

Key words. Galaxy: abundances – Galaxy: evolution – (Galaxy:) local interstellar matter – ISM: abundances – ISM: molecules – radio lines: ISM

1. Introduction

Isotopic abundance ratios of carbon, nitrogen, and oxygen (CNO elements) are commonly used to trace the chemical history from molecular clouds to planetary systems (e.g. Caselli & Ceccarelli 2012), as well as chemical enrichment and nucleosynthesis processes in galaxies (e.g. Romano et al. 2017). Nitrogen is the fifth most abundant element in the universe, and its isotopic ratio ($^{14}\text{N}/^{15}\text{N}$) is found to be 441 ± 6 for the proto-solar nebula in which our Sun was born (Marty et al. 2010). This value is higher than those measured in pristine Solar System material, such as comets (144 ± 3 ; Hily-Blant et al. 2017), and in carbonaceous chondrites of meteorites ($44-264$; van Kooten et al. 2017). Thus, there was an enrichment of ^{15}N during the formation of the Solar System, the causes of which are still unknown. Observations of different molecular clouds and star-forming regions show a spread in the $^{14}\text{N}/^{15}\text{N}$ ratios depending on the physical conditions and/or molecular species. $^{14}\text{N}/^{15}\text{N}$ ratios of $\sim 150-800$ have been found towards low-mass pre-stellar cores and protostellar objects, infrared dark clouds (IRDCs), and high-mass star-forming regions (e.g. Daniel et al. 2013; Hily-Blant et al. 2013a,b; Wampfler et al. 2014; Zeng et al. 2017; Colzi et al. 2018a,b). Moreover, Guzmán et al. (2017) find an $\text{HCN}/\text{HC}^{15}\text{N}$

ratio of 80–160 towards a sample of protoplanetary discs, similar to the value found in comets. Finally, $^{14}\text{N}/^{15}\text{N}$ ratios from N_2H^+ towards pre-stellar cores and some massive star-forming regions behave completely differently and are higher than 800 (e.g. Fontani et al. 2015; Redaelli et al. 2018).

In general, the $^{14}\text{N}/^{15}\text{N}$ ratio is known to be governed by local chemical processes and by stellar nucleosynthesis. As a local process, low-temperature isotopic-exchange reactions or different rate coefficients for isotope-substitute gas-phase reactions have been invoked to explain the observed values (e.g. Roueff et al. 2015; Wirstrom & Charnley 2018; Loison et al. 2019; Hily-Blant et al. 2020). However, recent observational works have highlighted the importance of isotope-selective photodissociation of N_2 in explaining the local variation in the $^{14}\text{N}/^{15}\text{N}$ ratios in massive molecular clouds, low-mass Class 0/I objects, IRDCs, and protoplanetary discs (Colzi et al. 2019; Bergner et al. 2020; Fontani et al. 2020, 2021; Hily-Blant et al. 2019; Evans et al. 2022; Spezzano et al. 2022), as suggested by chemical models (e.g. Furuya & Aikawa 2018; Visser et al. 2018; Lee et al. 2021).

Besides chemistry, the $^{14}\text{N}/^{15}\text{N}$ elemental ratio is governed by stellar nucleosynthesis, since the two elements are synthesised through different processes. Both ^{14}N and ^{15}N are pro-

duced by fast-rotating massive stars as primary elements at low metallicities (Meynet & Maeder 2002; Limongi & Chieffi 2018). Primary ^{14}N is also synthesised at the base of the convective envelope of asymptotic giant branch (AGB) stars (e.g. Renzini & Voli 1981; Izzard et al. 2004). Most of the ^{14}N production from intermediate-mass stars, though, is secondary due to cold CNO processing during the main sequence and in the H-burning shells of red giants at relatively high metallicities (e.g. Karakas & Lattanzio 2014). ^{15}N is likely mainly produced by novae on a Galactic scale (Matteucci & D’Antona 1991; Romano & Matteucci 2003; Romano et al. 2017), but a contribution to its production from massive stars triggered by proton ingestion in the He shell cannot be ruled out (Pignatari et al. 2015).

Galactic chemical evolution (GCE) models that include up-to-date stellar yields predict that the $^{14}\text{N}/^{15}\text{N}$ ratio across the disc first increases in the galactocentric distance range $R_{\text{GC}}=4\text{--}8$ kpc and then stays constant or even mildly decreases up to 16 kpc (Romano et al. 2019). The predictions from these models are confirmed by observations towards massive star-forming regions in the inner Galaxy ($R_{\text{GC}} \leq 12$ kpc; e.g. Adande & Ziurys 2012; Colzi et al. 2018b), but no observations had been available to constrain GCE models to the outermost part of the Galaxy ($R_{\text{GC}} > 12$ kpc).

In this work we present the first study of the $^{14}\text{N}/^{15}\text{N}$ ratio towards the outer Galaxy in the context of the CHEMical complexity in star-forming regions of the OUTER Galaxy (CHEMOUT) project (Fontani et al. 2022a, hereafter Paper I). The observations are performed towards a sample of 35 dense molecular clouds associated with IRAS colours typical of star-forming regions, clearly detected in $\text{H}_2\text{CO } J_{K_a, K_b}=2_{1,2}-1_{1,1}$ (Blair et al. 2008), and between 8.7 and 23.4 kpc from the Galactic centre. More information on the sources, such as their coordinates, heliocentric distances, and molecules detected, can be found in Paper I. Moreover, Fontani et al. (2022b) recently studied CH_3OH , H_2CO , and HCO emission towards 15 out of the 35 targets of the CHEMOUT sample (hereafter Paper II). In Sects. 2 and 3 we present the observations, the analysis, and the observational results. In Sect. 4, updated GCE models are presented. Finally, a discussion of the observational results, the comparison with GCE model predictions, and the conclusions from this work are given in Sect. 5.

2. Observations

This work is based on the observations done for the CHEMOUT project, described in Paper I, performed with the Institut de RadioAstronomie Millimétrique (IRAM) 30m telescope. In the analysis presented here, we have used the 3 mm observations that include the $J = 1 - 0$ transitions of H^{15}NC , HN^{13}C , H^{13}CN , and HC^{15}N . The observations were done with the Fast Fourier Transform Spectrometer (FTS) in the finest frequency resolution of 50 kHz, providing a velocity resolution of ~ 0.17 km s $^{-1}$ at 88 GHz. For this work all the spectra were smoothed to 0.34 km s $^{-1}$. The data were obtained with the wobbler-switching technique with a wobbler throw of 240'', which translates to physical sizes of 10–30 pc for the distances considered in this work (8.7–23.4 kpc), significantly larger than the expected molecular emission of the targeted species. Other details (e.g. pointing and focus, full spectral windows, telescope efficiencies, and weather conditions) are given in Paper I. The spectra have been converted from antenna temperature to main beam temperature (T_{MB} ; see Table 2 of Paper I). The noise achieved, σ , at the frequencies of the observed transitions is given in Appendix A for each source.

3. Analysis and observational results

3.1. Detection information

The spectroscopic information of H^{13}CN , HN^{13}C , and HC^{15}N is taken from the Cologne Database for Molecular Spectroscopy¹ (CDMS; Müller et al. 2001, 2005; Endres et al. 2016), and that of H^{15}NC from the Jet Propulsion Laboratory catalogue² (JPL; Pickett et al. 1998). The entry of H^{13}CN , based on the laboratory works of Fuchs et al. (2004), Cazzoli & Puzzarini (2005), and Maiwald et al. (2000), includes the hyperfine structure due to the ^{14}N nucleus. The entry of HN^{13}C is based on van der Tak et al. (2009); the entry of HC^{15}N is based on Fuchs et al. (2004) and Cazzoli et al. (2005); and the entry of H^{15}NC is based on Creswell et al. (1976) and Pearson et al. (1976). The rest frequencies of the $J=1-0$ transitions are: 86.3387 GHz ($F=1-1$), 86.3402 GHz ($F=2-1$), and 86.3423 GHz ($F=0-1$) for H^{13}CN , 87.0908 GHz for HN^{13}C , 86.0550 GHz for HC^{15}N , and 88.8657 GHz for H^{15}NC . More spectroscopic information can be found in Colzi et al. (2018b).

The observed spectra at the rest frequencies of $\text{HN}^{13}\text{C}(1-0)$, $\text{H}^{15}\text{NC}(1-0)$, $\text{H}^{13}\text{CN}(1-0)$, and $\text{HC}^{15}\text{N}(1-0)$, towards the 35 sources, are shown in Figs. B.1–B.4 (Appendix B). The three $\text{H}^{13}\text{CN}(1-0)$ hyperfine components, which are separated by 5 and 7 km s $^{-1}$, can be resolved towards all sources since the linewidths are narrower (0.7–3.6 km s $^{-1}$; see Sect. 3.3).

We consider a line detected when the integrated intensity signal-to-noise ratio (S/N) is >6 . Moreover, we consider a line tentatively detected when the integrated intensity S/N is between 4 and 6. $\text{H}^{13}\text{CN}(1-0)$ has been detected in 21 sources (60% of the total sample). The three hyperfine components are clearly detected towards six sources: WB89-379, WB89-391, WB89-437, WB89-621, 19423+2541, and WB89-060 (see Fig. B.3). Among the H^{13}CN detections, $\text{HC}^{15}\text{N}(1-0)$ has been detected in 14 sources (40% of the total sample). $\text{HN}^{13}\text{C}(1-0)$ has been detected in 18 sources (51% of the total sample), and $\text{H}^{15}\text{NC}(1-0)$ only in 3 of them ($\sim 9\%$ of the total sample).

The profile of the $\text{HN}^{13}\text{C}(1-0)$ transition, which is the only species detected towards WB89-670, shows an inverse P-Cygni profile, and this might suggest infall material towards the centre of the source. For visualisation purposes, we have fitted this line with two velocity components, one in emission and one in absorption assuming a continuum background temperature of 50 K. A similar profile was also observed in Paper I in HCO^+ and $\text{c-C}_3\text{H}_2$ towards the same source. As also found in Paper I for $\text{c-C}_3\text{H}_2$, towards 19383+2711 we detect two velocity components that are probably part of the same cloud. Conversely, for 19571+3113 we only detect the velocity component at -61 km s $^{-1}$ and not that at -66 km s $^{-1}$ (see Paper I).

3.2. Molecular line analysis

First, for each line we fitted the baseline with a polynomial function of maximum order 1. Then we used the Spectral Line Identification and Modeling (SLIM) tool within the MADCUBA package³ (Martín et al. 2019). SLIM generates a synthetic spectrum, assuming local thermodynamic equilibrium (LTE) conditions considering the line opacity, and applies the AUTOFIT algorithm to find the best non-linear least-square fit to the data.

¹ <http://cdms.astro.uni-koeln.de/classic/>

² <https://spec.jpl.nasa.gov/ftp/pub/catalog/catdir.html>

³ Madrid Data Cube Analysis on ImageJ is a software developed at the Center of Astrobiology (CAB) in Madrid; <https://cab.inta-csic.es/madcuba/>.

Table 1. Total column densities, $\text{H}^{13}\text{CN}/\text{HC}^{15}\text{N}$ and $\text{HN}^{13}\text{C}/\text{H}^{15}\text{NC}$ ratios, $^{14}\text{N}/^{15}\text{N}$ ratios, and galactocentric distances (R_{GC}).

Source	$N(\text{HN}^{13}\text{C})$ ($\times 10^{11} \text{ cm}^{-2}$)	$N(\text{H}^{15}\text{NC})$ ($\times 10^{11} \text{ cm}^{-2}$)	$N(\text{H}^{13}\text{CN})$ ($\times 10^{11} \text{ cm}^{-2}$)	$N(\text{HC}^{15}\text{N})$ ($\times 10^{11} \text{ cm}^{-2}$)	$\text{H}^{13}\text{CN}/\text{HC}^{15}\text{N}^a$ ($\text{HN}^{13}\text{C}/\text{H}^{15}\text{NC}$)	$\text{HCN}/\text{HC}^{15}\text{N}^a$ ($\text{HNC}/\text{H}^{15}\text{NC}$)	R_{GC} (kpc)
WB89-315	≤ 1.3	≤ 1.1	≤ 1.0	≤ 1.0	–	–	16.3
WB89-379	1.0 ± 0.2	≤ 0.5	6.2 ± 0.3	1.5 ± 0.2	$4.1 \pm 0.6 (\geq 2.1)$	$452 \pm 77 (\geq 232)$	16.4
WB89-380	1.6 ± 0.3^b	≤ 0.9	8.2 ± 0.5	2.0 ± 0.3	$4.1 \pm 0.7 (\geq 1.7)$	$447 \pm 90 (\geq 189)$	16.0
WB89-391	≤ 0.3	≤ 0.3	5.0 ± 0.2	1.0 ± 0.1	5.0 ± 0.6	546 ± 78	16.1
WB89-399	≤ 1.1	≤ 1.3	≤ 1.2	≤ 1.2	–	–	16.0
WB89-437	2.2 ± 0.4	≤ 1.0	15.5 ± 0.6	4.5 ± 0.4	$3.5 \pm 0.3 (\geq 2.1)$	$370 \pm 48 (\geq 226)$	15.7
WB89-440	≤ 0.6	≤ 0.8	≤ 0.7	≤ 0.7	–	–	15.7
WB89-501	≤ 0.5	≤ 0.5	2.3 ± 0.3	1.1 ± 0.4^b	2.1 ± 0.9	228 ± 101	15.6
WB89-529	≤ 1.2	≤ 1.6	≤ 1.3	≤ 1.4	–	–	17.8
WB89-572	≤ 0.5	≤ 0.6	1.7 ± 0.5^b	1.0 ± 0.2^b	1.6 ± 0.6	196 ± 73	18.3
WB89-621	1.4 ± 0.2	≤ 0.5	18.1 ± 0.5	3.2 ± 0.3	$5.6 \pm 0.6 (\geq 2.9)$	$703 \pm 86 (\geq 365)$	18.9
WB89-640	≤ 0.8	≤ 0.8	2.3 ± 0.5^b	≤ 0.8	≥ 2.8	≥ 312	16.8
WB89-670	1.0 ± 0.2^b	≤ 0.7	≤ 0.6	≤ 0.6	$-(\geq 1.4)$	$-(\geq 214)$	23.4
WB89-705	2.9 ± 0.3	≤ 0.8	≤ 0.6	≤ 0.6	$-(\geq 3.77)$	$-(\geq 510)$	20.5
WB89-789	2.7 ± 0.3	≤ 0.8	3.4 ± 0.5^b	3.4 ± 0.5	$1.0 \pm 0.2 (\geq 3.52)$	$127 \pm 30 (\geq 445)$	19.1
WB89-793	1.9 ± 0.7^b	≤ 1.6	≤ 1.5	≤ 0.9	$-(\geq 1.2)$	$-(\geq 137)$	16.9
WB89-898	≤ 1.0	≤ 1.2	1.5 ± 0.8^b	≤ 0.9	≥ 1.6	≥ 173	15.8
19423+2541	1.3 ± 0.2	1.3 ± 0.4^b	14.5 ± 0.5	2.7 ± 0.5	$5.3 \pm 0.9 (1.0 \pm 0.4)$	$492 \pm 99 (96 \pm 34)$	13.5
19383+2711	1.0 ± 0.2	≤ 0.5	7.6 ± 0.6	2.9 ± 0.4	$2.6 \pm 0.4 (\geq 1.9)$	$228 \pm 45 (\geq 173)$	12.7
19383+2711-b ^c	≤ 0.5	≤ 0.5	5.2 ± 0.6	≤ 1.3	≥ 4.1	≥ 373	13.2
19489+3030	1.9 ± 0.2	≤ 0.7	3.5 ± 0.5	≤ 0.7	$\geq 5.0 (\geq 2.8)$	$\geq 446 (\geq 254)$	12.9
19571+3113	1.3 ± 0.3^b	≤ 0.9	4.0 ± 0.5	1.1 ± 0.2	$3.6 \pm 0.9 (\geq 1.5)$	$311 \pm 85 (\geq 127)$	12.2
20243+3853	1.3 ± 0.3^b	≤ 0.7	6.0 ± 0.6	1.1 ± 0.2	$5.5 \pm 1.2 (\geq 1.8)$	$494 \pm 119 (\geq 159)$	12.8
WB89-002	≤ 1.2	≤ 1.6	≤ 1.3	≤ 1.3	–	–	8.7
WB89-006	2.7 ± 0.5	2.7 ± 0.6	2.7 ± 0.7^b	≤ 1.1	$\geq 2.5 (1.0 \pm 0.3)$	$\geq 246 (96 \pm 28)$	14.3
WB89-014	≤ 0.9	≤ 1.1	≤ 0.9	≤ 1.0	–	–	14.9
WB89-031	≤ 0.7	≤ 0.8	≤ 0.7	≤ 0.7	–	–	14.1
WB89-035	≤ 0.6	≤ 7.8	3.3 ± 0.5	≤ 0.6	≥ 5.4	≥ 492	13.1
WB89-040	0.60 ± 0.16^b	≤ 0.5	2.6 ± 0.4	≤ 0.5	$\geq 5.4 (\geq 1.1)$	$\geq 454 (\geq 97)$	11.9
WB89-060	2.0 ± 0.3	≤ 0.8	18.8 ± 0.7	3.0 ± 0.3	$6.3 \pm 0.7 (\geq 2.4)$	$595 \pm 87 (\geq 230)$	13.6
WB89-076	3.31 ± 0.18	1.2 ± 0.4^b	3.3 ± 0.4	1.07 ± 0.19	$3.1 \pm 0.6 (2.7 \pm 0.8)$	$318 \pm 71 (275 \pm 87)$	15.1
WB89-080	≤ 1.2	≤ 1.5	≤ 1.3	≤ 1.2	–	–	12.8
WB89-083	0.70 ± 0.08	≤ 0.4	≤ 0.4	≤ 0.4	$-(\geq 1.8)$	$-(\geq 182)$	14.7
WB89-152	≤ 1.0	≤ 1.1	≤ 1.1	≤ 1.1	–	–	14.4
WB89-283	≤ 0.3	≤ 0.4	1.1 ± 0.3^b	≤ 0.4	≥ 2.6	≥ 278	15.8
WB89-288	≤ 0.6	≤ 0.4	≤ 0.4	0.6 ± 0.2^b	≤ 0.6	≤ 71	16.8

Notes. Column densities have been derived assuming a T_{ex} of 25 K (see Sect. 3.2). Column density errors do not take the calibration error ($\sim 10\%$) into account. The calibration error for the $^{14}\text{N}/^{15}\text{N}$ ratio largely cancels out as the corresponding pairs of lines are recorded with the same spectral setup. ^(a) Ratios derived from HNC are also indicated in parentheses, when derived. ^(b) Tentative detection. ^(c) Second velocity component at $v_{\text{LSR}} = -71.2 \text{ km s}^{-1}$, derived from the $\text{H}^{13}\text{CN}(1-0)$ line peak (see Table A.3).

The free parameters that are considered in the fit are the column density of the molecule, N , the excitation temperature, T_{ex} , the velocity, v_{LSR} , and the full width half maximum (FWHM; see details in Martín et al. 2019).

The column densities were evaluated assuming that the emission fills the telescope beam (i.e. no beam dilution has been applied) since we do not have any size measurement of the emitting region of these lines in this sample of sources. Therefore, the derived column densities are beam-averaged values. For the analysis of H^{13}CN , we considered the three hyperfine components to perform the fit with SLIM. The T_{ex} of the targeted molecules cannot be derived since we have a single rotational transition. We thus assumed that the $J=1-0$ rotational levels of the four molecules (H^{13}CN , HC^{15}N , HN^{13}C , and H^{15}NC) are

populated with the same T_{ex} . The non-LTE calculations performed by Colzi et al. (2018b) on a sample of star-forming regions in the inner Galaxy showed that this is a reasonable assumption, since the T_{ex} of the $J=1-0$ transitions of the molecules differ only within $\sim 16\%$ (see their Sect. 3.2). For the fit procedure we assumed a T_{ex} of 25 K for all the sources analysed, and hence the column density derived (see Table 1) corresponds to this temperature. However, we note that while the column densities of the individual species depend on T_{ex} , their ratios, which are the main goal of the work, are almost independent of it. As discussed by Colzi et al. (2018a), the $^{14}\text{N}/^{15}\text{N}$ derived from the $J=1-0$ rotational transition does not depend significantly on the assumed T_{ex} . The analysis of other molecules for which multiple transitions have been detected towards this sample (CH_3CCH

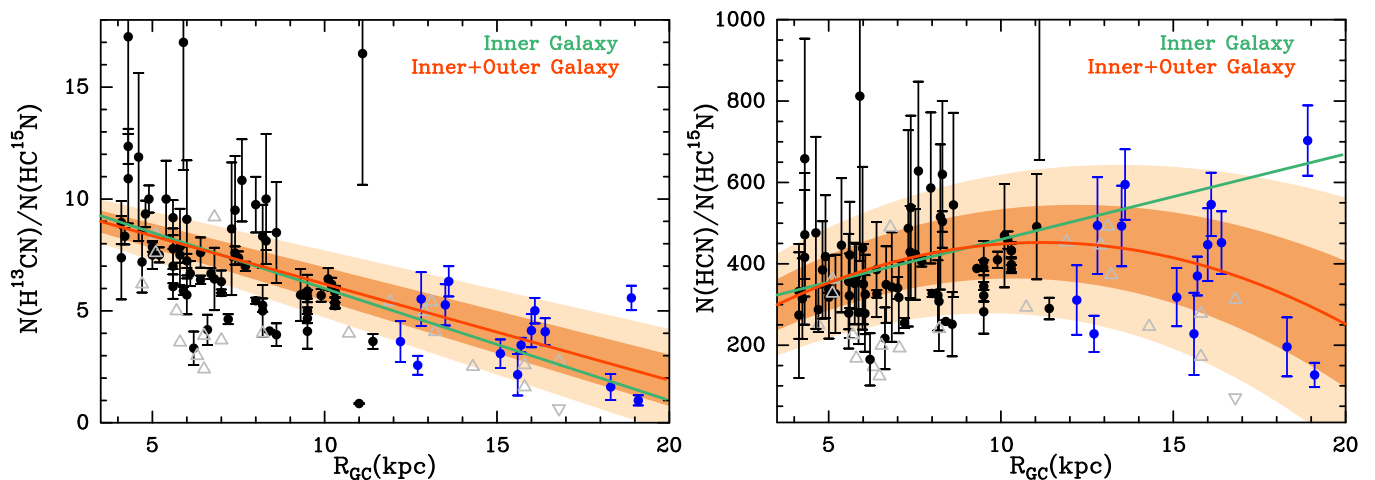


Fig. 1. Isotopic ratios vs. galactocentric distance. *Left panel:* $\text{H}^{13}\text{CN}/\text{HC}^{15}\text{N}$ ratio as a function of the galactocentric distance, R_{GC} . The solid red line is the linear regression fit obtained using the whole sample, along with its 0.5σ and 1σ uncertainty (dark and light orange regions, respectively). *Right panel:* Same as the left panel but for the $^{14}\text{N}/^{15}\text{N}$ ratio of HCN. The solid red parabola is obtained from the analysis of the data, as explained in Sect. 3.3, along with its 0.5σ and 1σ uncertainty (dark and light orange regions, respectively). In both panels the solid green line represents the linear trend found in the inner Galaxy by Colzi et al. (2018b) and extrapolated up to 20 kpc. Black points represent the values obtained in the inner Galaxy by Colzi et al. (2018b), and blue points are the values obtained in this work towards the outer Galaxy. Grey triangles pointing upwards are lower limits, while those pointing downwards are upper limits. Note that the source at $R_{GC}=2.1$ kpc from Colzi et al. (2018b) has been used for the analysis but is not shown in this plot for visualisation purposes.

and CH_3OH) have provided values of $T_{\text{ex}}=7\text{--}27$ K (Paper I and II, respectively). These species can be used as thermometers and are expected to trace an extended molecular envelope similar to that traced by HCN. Using this range as a guide, we explored how the assumption of T_{ex} affects the derived molecular column density ratios. By changing the assumed T_{ex} between 5 K and 30 K, we find that the $\text{H}^{13}\text{CN}/\text{HC}^{15}\text{N}$ ratio only varies between 1% and 10% with respect to the values obtained with $T_{\text{ex}} = 25$ K. The SLIM fit also provides an estimate of the line opacities and confirms that the transitions of all the isotopologues are optically thin. Upper limits on column densities were also derived for undetected lines. They were determined taking the 3σ root mean square of the spectra at the observed rest frequencies into account (see Appendix A) and assuming the FWHM. The latter was considered to be equal to that of the other corresponding isotopologue (e.g. that of H^{13}CN for the upper limit of HC^{15}N), if detected, or to that of the other molecules (e.g. that of HN^{13}C or H^{15}NC , or the average of the two, for the upper limit of HC^{15}N) for the same source. If none of the four molecules have been detected, we assumed the same FWHM as that of $\text{c-C}_3\text{H}_2$, which is detected in all of the sources, except WB89–315 for which we used the FWHM of HCO^+ . Moreover, for upper limits, the v_{LSR} was assumed to be equal to the velocity, v_0 , obtained from H_2CO observations by Blair et al. (2008) (see Paper I and Fig. B.1).

3.3. Results

The results from the fit procedure are listed in Tables A.1, A.2, A.3, and A.4 for $\text{HN}^{13}\text{C}(1\text{--}0)$, $\text{H}^{15}\text{NC}(1\text{--}0)$, $\text{H}^{13}\text{CN}(1\text{--}0)$, and $\text{HC}^{15}\text{N}(1\text{--}0)$, respectively. Total column densities, $\text{H}^{13}\text{CN}/\text{HC}^{15}\text{N}$ and $\text{HN}^{13}\text{C}/\text{H}^{15}\text{NC}$ ratios, and R_{GC} are listed in Table 1. We derived the $^{14}\text{N}/^{15}\text{N}$ ratios by multiplying $\text{H}^{13}\text{CN}/\text{HC}^{15}\text{N}$ and $\text{HN}^{13}\text{C}/\text{H}^{15}\text{NC}$ by $^{12}\text{C}/^{13}\text{C}$ as a function of the R_{GC} derived by Milam et al. (2005) for CN, which is a nitrile species, as are HCN and HNC:

$$^{12}\text{C}/^{13}\text{C} = (6.01 \pm 1.19) \text{ kpc}^{-1} \times R_{GC} + (12.28 \pm 9.33). \quad (1)$$

Other similar galactocentric trends, which are consistent within the associated uncertainties, have also been derived using H_2CO and CO (Milam et al. 2005; Yan et al. 2019). Since in this work we analyse nitriles and isonitriles, we adopted the trend obtained from CN shown in Eq. 1. This relation was obtained for the inner Galaxy, so its extrapolation to the outer Galaxy is uncertain. To our best knowledge there are no observational studies of the behaviour of the $^{12}\text{C}/^{13}\text{C}$ ratio with R_{GC} in the outer Galaxy towards a large sample of sources. Wouterloot & Brand (1996) derived the $^{13}\text{CO}/\text{C}^{18}\text{O}$ ratio towards only five sources (WB89-380, WB89-391, WB89-399, WB89-437, and WB89-501, whose R_{GC} are about 16 kpc; see Table 1), and they found $^{13}\text{CO}/\text{C}^{18}\text{O}$ ratios in the range 12–17.5. These values can be converted to the $^{12}\text{C}/^{13}\text{C}$ ratio assuming a value of $^{16}\text{O}/^{18}\text{O}$. Although this ratio has not been studied observationally in the outer Galaxy, GCE models (Romano et al. 2017) predict values of ~ 2000 . This leads to a $^{12}\text{C}/^{13}\text{C}$ ratio for CO of 115–170, significantly higher than the local value of ~ 70 . Moreover, Wouterloot & Brand (1996) directly derived a $^{12}\text{C}/^{13}\text{C}$ ratio of 200 ± 15 towards WB89-437 from $\text{C}^{18}\text{O}/^{13}\text{C}^{18}\text{O}$. Milam et al. (2005) also studied the $^{12}\text{C}/^{13}\text{C}$ ratio towards WB89-391 and found a value of 134 ± 43 for CN, in very good agreement with that of CO (~ 132) obtained by Wouterloot & Brand (1996). These estimates suggest that the $^{12}\text{C}/^{13}\text{C}$ ratio keeps increasing in the outer Galaxy, in good agreement with the extrapolation of the galactocentric trend of Eq. (1). We stress that this is also supported by the predictions from GCE models, as described in more detail in Sect. 4 and Appendix C. Hence, we have assumed that the linear trend of Eq. 1 is also valid for the outer Galaxy, as we did for the inner Galaxy in Colzi et al. (2018b).

The uncertainties of the $^{14}\text{N}/^{15}\text{N}$ ratios were evaluated by considering the uncertainty given by the fit procedure and propagating it by also taking Eq. (1) into account. The final $^{14}\text{N}/^{15}\text{N}$ ratios obtained are listed in Table 1. Since H^{15}NC has only been detected in three sources, the galactocentric trends and the comparison with GCE models are discussed just for HCN from now on.

The left panel of Fig. 1 shows the $\text{H}^{13}\text{CN}/\text{HC}^{15}\text{N}$ ratio as a function of R_{GC} for the sources with R_{GC} from 12 kpc to 19 kpc derived in this work, and for those with R_{GC} between 2 kpc and 12 kpc from Colzi et al. (2018b). For the entire set of data we performed an unweighted linear regression fit and find

$$\text{H}^{13}\text{CN}/\text{HC}^{15}\text{N} = (-0.43 \pm 0.08) \text{ kpc}^{-1} \times R_{\text{GC}} + (10.5 \pm 0.7). \quad (2)$$

This fit is very similar to the extrapolation of the linear trend found by Colzi et al. (2018b) in the inner Galaxy (see the red line with respect to the green line in the left panel of Fig. 1).

The right panel of Fig. 1 shows the $^{14}\text{N}/^{15}\text{N}$ ratios of HCN as a function of R_{GC} . Most of the observed points in the outer Galaxy stay clearly below the extrapolation up to 20 kpc of the linear $^{14}\text{N}/^{15}\text{N}$ trend obtained in the inner Galaxy by Colzi et al. (2018b). This indicates that the increasing $^{14}\text{N}/^{15}\text{N}$ ratio with R_{GC} found in the inner Galaxy is not valid beyond 10-12 kpc. Indeed, the observed $^{14}\text{N}/^{15}\text{N}$ values in the outer Galaxy decrease with R_{GC} , with the only exception being WB89-621, which presents a $^{14}\text{N}/^{15}\text{N}$ ratio of ~ 700 at 18.9 kpc. This source is one of the most luminous and massive of the sample (see Paper I and Elia et al. 2021), suggesting the presence of a proto-cluster whose chemistry could affect the $^{14}\text{N}/^{15}\text{N}$ ratio. However, higher-angular-resolution observations are needed to draw conclusions.

Following the analysis done by Colzi et al. (2018b) for the inner Galaxy, and multiplying Eq. (2) by Eq. (1), a parabolic trend is obtained (see the red curve in the right panel of Fig. 1, where the 0.5σ and 1σ uncertainties are also shown), with a maximum at ~ 11 kpc:

$$\text{HCN}/\text{HC}^{15}\text{N} = -2.58 \text{ kpc}^{-2} \times R_{\text{GC}}^2 + 57.82 \text{ kpc}^{-1} \times R_{\text{GC}} + 128.94. \quad (3)$$

In Appendix D we also look for azimuthal $^{14}\text{N}/^{15}\text{N}$ ratio variations as already done in the inner Galaxy by Colzi et al. (2018b). No trend within the spiral arms is found (see Fig. D.1).

4. Galactic chemical evolution models

To understand the galactocentric trend observed, we studied the evolution of the chemical composition of the interstellar medium in the Galactic disc at different R_{GC} using the chemical evolution model described in Grisoni et al. (2017, 2018) and Romano et al. (2021). According to this model, the Milky Way disc forms inside-out (Matteucci & François 1989) with a higher star-formation efficiency in the inner regions, such that a metallicity gradient is naturally established, as observed (e.g. Méndez-Delgado et al. 2022).

The adopted nucleosynthesis prescriptions follow Romano et al. (2019, 2021), with some updates (Romano et al., in prep.). For single low- and intermediate-mass stars ($1 \leq M/M_{\odot} < 9$), we adopted the yields of Ventura et al. (2013, 2014, 2018, 2020, 2021) that cover all metallicity regimes, from the ultra metal-poor to the super-solar. The adopted yields include the effects of dredge ups, hot bottom burning, and mass loss, as well as a proper treatment of the super-AGB phase for the most massive stars. The yields of single massive stars ($13 \leq M/M_{\odot} \leq 100$) that end their lives as core-collapse supernovae are taken from Limongi & Chieffi (2018). In particular, for $[\text{Fe}/\text{H}] < -1$ dex we used their ‘set R’ (see Limongi & Chieffi 2018 for details), assuming that all stars have initial rotation velocities $v_{\text{rot}} = 300 \text{ km s}^{-1}$. For higher

Table 2. GCE model prescriptions.

Model	Mass range for WD ^a progenitors (M_{\odot})	$M_{\text{ejec}}^{13\text{C}}$ (M_{\odot})	$M_{\text{ejec}}^{15\text{N}}$ (M_{\odot})	Flag
1	1–8	$5.40\text{e-}7$	$3.35\text{e-}8$	dark green
2	1–8	$6.40\text{e-}7$	$3.95\text{e-}8$	light green
3	3–8	$3.25\text{e-}7$	$1.91\text{e-}8$	magenta
4	3–8	$4.25\text{e-}7$	$2.40\text{e-}8$	pink

Notes. Col. 2: mass range of primary stars in nova systems; Cols. 3 and 4: average ejected masses of ^{13}C and ^{15}N per nova outburst. ^(a) White dwarf.

metallicities ($[\text{Fe}/\text{H}] \geq -1$) we assumed the yields for non-rotating stars. The mass limit for full collapse to black holes is set to $30 M_{\odot}$ if $[\text{Fe}/\text{H}] < -1$ and to $60 M_{\odot}$ if $[\text{Fe}/\text{H}] \geq -1$. These choices allow us to reproduce satisfactorily well the evolution of the stable CNO isotopes in the Galaxy (Romano et al. 2019; Romano et al., in prep.).

The model implements ^{13}C and ^{15}N production from nova systems following Romano et al. (2017, 2021). First, the rate of formation of nova systems at any time is computed as a fraction, α , of the white dwarf (WD) birth rate at a previous time, taking into account the delay needed for the WDs to cool to a temperature that ensures strong enough nova outbursts (~ 1 Gyr). The free parameter α is assumed to be constant in time, and its value was set as to reproduce the current nova rate in the Galaxy of $R_{\text{nova}}(t_{\text{now}}) \simeq 35 \text{ yr}^{-1}$ (De et al. 2021). In computing the theoretical nova rate, it was assumed that each nova suffers 10^4 outbursts during its lifetime (Bath & Shaviv 1978); for the sake of simplicity, the outbursts were assumed to occur instantaneously. The average masses ejected in the form of ^{13}C and ^{15}N by each nova were fixed by the request that the relevant CNO isotope observations be reproduced; they are listed in Table 2. We caution that there is a high degeneracy in the suggested nova yields due to the uncertain current Galactic nova rate (e.g. De et al. 2021; Rector et al. 2022).

The four models presented in this work are summarised in Table 2. We ran models in which the nova system WD progenitors have initial masses in the range $1\text{--}8 M_{\odot}$ and models in which only the most massive WDs (originating from stars in the range $3\text{--}8 M_{\odot}$) have the right characteristics to produce nova outbursts (see Romano et al. 2021). The predicted gradients are compared to the observational trends in Fig. 2. We further considered different values of the masses ejected in the form of ^{13}C and ^{15}N in each outburst (see Table 2). In fact, rather than providing a ‘best-fitting curve’, we aimed to show a ‘permitted area’. We stress that the nova yields listed in Table 2 are linked to the assumed current nova rate (35 yr^{-1}). Should the rate be sensibly higher or lower than this (e.g. De et al. 2021; Rector et al. 2022), the yields would have to be changed accordingly. For the sake of completeness, we also present the predicted $^{12}\text{C}/^{13}\text{C}$ gradient in Appendix C, which is in good agreement with the observational trend we have used in this work, from Milam et al. (2005).

5. Discussion and conclusions

In this work we have studied, for the first time, the $^{14}\text{N}/^{15}\text{N}$ ratio towards 35 star-forming regions located in the outer Galaxy ($R_{\text{GC}} > 12$ kpc). We have derived the $\text{H}^{13}\text{CN}/\text{HC}^{15}\text{N}$ ratio towards 14 of them and the $\text{HN}^{13}\text{C}/\text{H}^{15}\text{NC}$ ratio for 3 sources. We

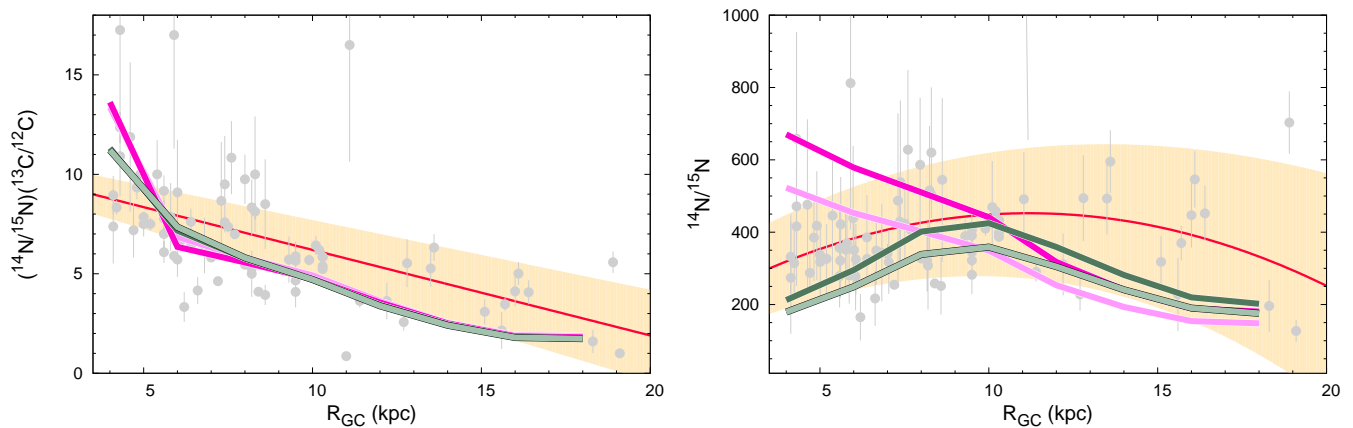


Fig. 2. Isotopic ratios predicted by GCE models. *Left panel:* Comparison between the $(^{14}\text{N}/^{15}\text{N}) \times (^{13}\text{C}/^{12}\text{C})$ ratios derived from observations and predicted by GCE models. The red line and light orange regions are the same as in Fig. 1. *Right panel:* Same as the left panel, but for the $^{14}\text{N}/^{15}\text{N}$ ratio. In both panels grey points correspond to the observed star-forming regions. The dark green, light green, magenta, and pink lines are the predictions from GCE models (see Sect. 4 and Table 2). Note that in the left panel the dark green model is below the light green one.

have observed a clearly decreasing trend of the $\text{H}^{13}\text{CN}/\text{HC}^{15}\text{N}$ ratio with increasing R_{GC} [Eq. (2)], also taking previous observations of the inner Galaxy by Colzi et al. (2018b) into account. This decreasing trend has a very similar slope as that found previously only in the inner Galaxy. Extrapolating the linear positive $^{12}\text{C}/^{13}\text{C}$ trend derived by Milam et al. 2005 to the outer Galaxy, which is supported by GCE models, the $^{14}\text{N}/^{15}\text{N}$ ratio shows a parabolic trend increasing up to 11 kpc and then decreasing for larger galactocentric distances [Eq. (3)].

If ^{15}N is produced during nova outbursts on long timescales (≥ 1 Gyr), as assumed in the adopted GCE models⁴, the observed trend of increasing $^{14}\text{N}/^{15}\text{N}$ when moving from the inner Galaxy to the solar circle, and decreasing $^{14}\text{N}/^{15}\text{N}$ when moving from the solar radius to the outer disc, can be reproduced. In particular, if low-mass stars ($M < 1.5 M_{\odot}$) enter the formation of nova systems, significant ^{15}N pollution is expected in the inner Galaxy from $M \sim 1 M_{\odot}$ stars that formed in large number in the early Milky Way, due to the very efficient star-formation rates and faster formation of these regions. In the outer Galaxy, which suffers low-level star formation and slow gas accretion from the intergalactic medium (inside-out formation), the effect is reduced. In fact, the differences between the case in which low- and intermediate-mass stars enter the formation of nova systems with respect to that in which this occurs only for intermediate-mass stars are minimal (cf. magenta and pink versus green curves in Fig. 2). The decrease in the $^{14}\text{N}/^{15}\text{N}$ ratio in the outer Galaxy, on the other hand, is dictated by the nucleosynthesis prescriptions for single low- and intermediate-mass stars: Romano et al. (2019) show that a decreasing trend has to be expected in the outer Galaxy when adopting the stellar yields of Ventura et al. (2013, 2014, 2018, 2020, 2021) due to the strong metal dependence of the ^{14}N yield in this case. Their predictions are confirmed by the observations presented in this work. As shown in Appendix C, GCE simulations predict that the $^{12}\text{C}/^{13}\text{C}$ ratio also keeps increasing with R_{GC} in the outer Galaxy, independently of the assumed model (Fig. C.1 in Appendix C). This is consistent with the assumption we made a priori to evaluate the $^{14}\text{N}/^{15}\text{N}$ ratios (Sect. 3.3) from the observed $\text{H}^{13}\text{CN}/\text{HC}^{15}\text{N}$ ratios. However, this theoretical prediction needs

to be confirmed with more observations of the $^{12}\text{C}/^{13}\text{C}$ ratio in the outer Galaxy.

While the general galactocentric behaviour of the $^{14}\text{N}/^{15}\text{N}$ ratio can be mainly explained by nucleosynthesis effects, its scatter at each galactocentric distance could be associated with local chemical fractionation effects, such as isotope selective photodissociation of N_2 (e.g. Furuya & Aikawa 2018), as mentioned in Sect. 1. We are not able to discuss this point in more detail since physical properties, such as H_2 densities, kinetic temperatures, and the possible presence of protostellar objects, are not available – or not well constrained – for all objects at present. It is clear from these new observations in the outer Galaxy that nitrogen fractionation effects, if present, are not systematic or dominant in the outer Galaxy, as already found in the inner Galaxy. This is true for the spatial scales studied in these works (~ 0.2 – 2 pc). In fact, the average trend with R_{GC} is consistent – within the associated uncertainties – with the predictions of GCE models that take stellar nucleosynthesis effects into account but do not account for chemical processes acting in molecular clouds. Higher-angular-resolution observations would be needed for each source to disentangle the local contribution from the nucleosynthetic one.

Acknowledgements. We thank the anonymous referee for the careful reading of the article and the useful comments. This work is based on observations carried out under projects number 116-17 and 004-18 with the IRAM 30m telescope. IRAM is supported by INSU/CNRS (France), MPG (Germany) and IGN (Spain). F.F. is grateful to the IRAM 30m staff for their precious help during the observations. L.C. acknowledges financial support through the Spanish grant PID2019-105552RB-C41 funded by MCIN/AEI/10.13039/501100011033. V.M.R. has received support from the Comunidad de Madrid through the Atracción de Talento Investigador Modalidad 1 (Doctores con experiencia) Grant (COOL: Cosmic Origins of Life; 2019-T1/TIC-5379), and the Ayuda RYC2020-029387-I funded by MCIN/AEI/10.13039/501100011033. This publication has received funding from the European Union Horizon 2020 research and innovation programme under grant agreement No 730562 (RadioNet).

References

- Adande, G. R. & Ziurys, L. M. 2012, *ApJ*, 744, 194
 Bath, G. T. & Shaviv, G. 1978, *MNRAS*, 183, 515
 Bergner, J. B., Öberg, K. I., Bergin, E. A., et al. 2020, *ApJ*, 898, 97
 Blair, S. K., Magnani, L., Brand, J., & Wouterloot, J. G. A. 2008, *Astrobiology*, 8, 59
 Caselli, P. & Ceccarelli, C. 2012, *A&A Rev.*, 20, 56
 Cazoli, G. & Puzzarini, C. 2005, *Journal of Molecular Spectroscopy*, 233, 280

⁴ Novae are also necessary to explain ^7Li enrichment in the Galaxy (e.g. Romano et al. 2021, and references therein).

- Cazzoli, G., Puzzarini, C., & Gauss, J. 2005, *ApJS*, 159, 181
- Colzi, L., Fontani, F., Caselli, P., et al. 2018a, *A&A*, 609, A129
- Colzi, L., Fontani, F., Caselli, P., et al. 2019, *MNRAS*, 485, 5543
- Colzi, L., Fontani, F., Rivilla, V. M., et al. 2018b, *MNRAS*, 478, 3693
- Creswell, R. A., Pearson, E. F., Winnewisser, M., & Winnewisser, G. 1976, *Zeitschrift Naturforschung Teil A*, 31, 221
- Daniel, F., Gérin, M., Roueff, E., et al. 2013, *A&A*, 560, A3
- De, K., Kasliwal, M. M., Hankins, M. J., et al. 2021, *ApJ*, 912, 19
- Elia, D., Merello, M., Molinari, S., et al. 2021, *MNRAS*, 504, 2742
- Endres, C. P., Schlemmer, S., Schilke, P., Stutzki, J., & Müller, H. S. P. 2016, *Journal of Molecular Spectroscopy*, 327, 95
- Evans, L., Fontani, F., Vastel, C., et al. 2022, *A&A*, 657, A136
- Fontani, F., Barnes, A. T., Caselli, P., et al. 2021, *MNRAS*, 503, 4320
- Fontani, F., Caselli, P., Palau, A., Bizzocchi, L., & Ceccarelli, C. 2015, *ApJ*, 808, L46
- Fontani, F., Colzi, L., Bizzocchi, L., et al. 2022a, *A&A*, 660, A76
- Fontani, F., Quiaia, G., Ceccarelli, C., et al. 2020, *MNRAS*, 493, 3412
- Fontani, F., Schmiedecke, A., Sánchez-Monge, A., et al. 2022b, *A&A*, 664, A154
- Fuchs, U., Bruenken, S., Fuchs, G. W., et al. 2004, *Zeitschrift Naturforschung Teil A*, 59, 861
- Furuya, K. & Aikawa, Y. 2018, *ApJ*, 857, 105
- Grisoni, V., Spitoni, E., & Matteucci, F. 2018, *MNRAS*, 481, 2570
- Grisoni, V., Spitoni, E., Matteucci, F., et al. 2017, *MNRAS*, 472, 3637
- Guzmán, V. V., Öberg, K. I., Huang, J., Loomis, R., & Qi, C. 2017, *ApJ*, 836, 30
- Hily-Blant, P., Bonal, L., Faure, A., & Quirico, E. 2013a, *Icarus*, 223, 582
- Hily-Blant, P., Magalhaes, V., Kastner, J., et al. 2017, *A&A*, 603, L6
- Hily-Blant, P., Magalhaes de Souza, V., Kastner, J., & Forveille, T. 2019, *A&A*, 632, L12
- Hily-Blant, P., Pineau des Forêts, G., Faure, A., & Flower, D. R. 2020, *A&A*, 643, A76
- Hily-Blant, P., Pineau des Forêts, G., Faure, A., Le Gal, R., & Padovani, M. 2013b, *A&A*, 557, A65
- Izzard, R. G., Tout, C. A., Karakas, A. I., & Pols, O. R. 2004, *MNRAS*, 350, 407
- Karakas, A. I. & Lattanzio, J. C. 2014, *PASA*, 31, e030
- Lee, S., Nomura, H., Furuya, K., & Lee, J.-E. 2021, *ApJ*, 908, 82
- Limongi, M. & Chieffi, A. 2018, *ApJS*, 237, 13
- Loison, J.-C., Wakelam, V., Gratier, P., & Hickson, K. M. 2019, *MNRAS*, 484, 2747
- Maiwald, F., Lewen, F., Ahrens, V., et al. 2000, *Journal of Molecular Spectroscopy*, 202, 166
- Martín, S., Martín-Pintado, J., Blanco-Sánchez, C., et al. 2019, *A&A*, 631, A159
- Marty, B., Zimmermann, L., Burnard, P. G., et al. 2010, *Geochim. Cosmochim. Acta*, 74, 340
- Matteucci, F. & D'Antona, F. 1991, *A&A*, 247, L37
- Matteucci, F. & François, P. 1989, *MNRAS*, 239, 885
- Méndez-Delgado, J. E., Amayo, A., Arellano-Córdova, K. Z., et al. 2022, *MNRAS*, 510, 4436
- Meynet, G. & Maeder, A. 2002, *A&A*, 390, 561
- Milam, S. N., Savage, C., Brewster, M. A., Ziurys, L. M., & Wyckoff, S. 2005, *ApJ*, 634, 1126
- Müller, H. S. P., Schlöder, F., Stutzki, J., & Winnewisser, G. 2005, *Journal of Molecular Structure*, 742, 215
- Müller, H. S. P., Thorwirth, S., Roth, D. A., & Winnewisser, G. 2001, *A&A*, 370, L49
- Pearson, E. F., Creswell, R. A., Winnewisser, M., & Winnewisser, G. 1976, *Zeitschrift Naturforschung Teil A*, 31, 1394
- Pickett, H. M., Poynter, R. L., Cohen, E. A., et al. 1998, *J. Quant. Spectr. Rad. Transf.*, 60, 883
- Pignatari, M., Zinner, E., Hoppe, P., et al. 2015, *ApJ*, 808, L43
- Rector, T. A., Shafter, A. W., Burris, W. A., et al. 2022, *ApJ*, 936, 117
- Redaelli, E., Bizzocchi, L., Caselli, P., et al. 2018, *A&A*, 617, A7
- Reid, M. J., Menten, K. M., Brunthaler, A., et al. 2014, *ApJ*, 783, 130
- Renzini, A. & Voli, M. 1981, *A&A*, 94, 175
- Romano, D., Magrini, L., Randich, S., et al. 2021, *A&A*, 653, A72
- Romano, D. & Matteucci, F. 2003, *MNRAS*, 342, 185
- Romano, D., Matteucci, F., Zhang, Z.-Y., Ivison, R. J., & Ventura, P. 2019, *MNRAS*, 490, 2838
- Romano, D., Matteucci, F., Zhang, Z. Y., Papadopoulos, P. P., & Ivison, R. J. 2017, *MNRAS*, 470, 401
- Roueff, E., Loison, J. C., & Hickson, K. M. 2015, *A&A*, 576, A99
- Spezzano, S., Caselli, P., Sipilä, O., & Bizzocchi, L. 2022, *A&A*, 664, L2
- van der Tak, F. F. S., Müller, H. S. P., Harding, M. E., & Gauss, J. 2009, *A&A*, 507, 347
- van Kooten, E. M. M. E., Nagashima, K., Kasama, T., et al. 2017, *Geochim. Cosmochim. Acta*, 205, 119
- Ventura, P., Dell'Agli, F., Lugaro, M., et al. 2020, *A&A*, 641, A103
- Ventura, P., Dell'Agli, F., Romano, D., et al. 2021, *A&A*, 655, A6
- Ventura, P., Di Criscienzo, M., Carini, R., & D'Antona, F. 2013, *MNRAS*, 431, 3642
- Ventura, P., di Criscienzo, M., D'Antona, F., et al. 2014, *MNRAS*, 437, 3274
- Ventura, P., Karakas, A., Dell'Agli, F., García-Hernández, D. A., & Guzman-Ramirez, L. 2018, *MNRAS*, 475, 2282
- Visser, R., Bruderer, S., Cazzoletti, P., et al. 2018, *A&A*, 615, A75
- Wampfler, S. F., Jørgensen, J. K., Bizzarro, M., & Bisschop, S. E. 2014, *A&A*, 572, A24
- Wirström, E. S. & Charnley, S. B. 2018, *MNRAS*, 474, 3720
- Wouterloot, J. G. A. & Brand, J. 1996, *A&AS*, 119, 439
- Yan, Y. T., Zhang, J. S., Henkel, C., et al. 2019, *ApJ*, 877, 154
- Zeng, S., Jiménez-Serra, I., Cosentino, G., et al. 2017, *A&A*, 603, A22

Appendix A: Fit results

In this appendix the results of the fitting procedure for the $\text{HN}^{13}\text{C}(1-0)$, $\text{H}^{15}\text{NC}(1-0)$, $\text{H}^{13}\text{CN}(1-0)$, and $\text{HC}^{15}\text{N}(1-0)$ lines of all sources are shown. A T_{ex} of 25 K has been assumed for all the sources and molecules. The line analysis is explained in Sect. 3.2.

Table A.1. Results from the LTE fitting procedure described in Sect. 3.2 for $\text{HN}^{13}\text{C}(1-0)$.

Source	v_{LSR} (km s^{-1})	FWHM (km s^{-1})	$\int T_{\text{MB}} dv$ (mK km s^{-1})	σ (mK)
WB89-315	-95.1	2.1	≤ 32	13.0
WB89-379	-89.1 ± 0.2	2.2 ± 0.5	33 ± 13	5.8
WB89-380	-85.7 ± 0.3	3.0 ± 0.7	50 ± 20^a	7.0
WB89-391	-85.71	1.1	≤ 11	6.0
WB89-399	-82.2	2.2	≤ 36	14.0
WB89-437	-71.4 ± 0.3	3.2 ± 0.6	70 ± 23	7.4
WB89-440	-72.2	1.6	≤ 20	9.0
WB89-501	-58.4	1.3	≤ 16	8.0
WB89-529	-60.1	1.9	≤ 39	11.0
WB89-572	-48.0	0.7	≤ 17	12.0
WB89-621	-25.40 ± 0.07	0.98 ± 0.16	45 ± 13	6.6
WB89-640	-25.4	0.9	≤ 27	16.0
WB89-670	-17.72 ± 0.06	0.55 ± 0.15	32 ± 13^a	14.0
WB89-705	-12.16 ± 0.05	0.86 ± 0.11	91 ± 21	12.0
WB89-789	34.39 ± 0.08	1.39 ± 0.19	87 ± 20	10.0
WB89-793	30.0 ± 0.3	1.7 ± 0.7	61 ± 44^a	16.0
WB89-898	63.4	2.3	≤ 28	11.0
19423+2541	-71.9 ± 0.2	2.2 ± 0.5	42 ± 16	6.0
19383+2711	-65.74 ± 0.18	1.6 ± 0.4	31 ± 15	6.5
19383+2711-b	-71.2	1.6	≤ 16	6.5
19489+3030	-69.18 ± 0.07	1.11 ± 0.17	60 ± 16	10.5
19571+3113	-61.0 ± 0.3	2.34 ± 0.7	41 ± 19^a	8.2
20243+3853	-73.5 ± 0.4	2.96 ± 0.9	41 ± 20^a	7.0
WB89-002	-2.8	1.3	≤ 37	19.0
WB89-006	-91.0 ± 0.2	2.4 ± 0.5	86 ± 29	12.4
WB89-014	-96.0	1.7	≤ 28	12.6
WB89-031	-89.4	1.6	≤ 21	10.0
WB89-035	-77.7	2.2	≤ 19	7.5
WB89-040	-62.18 ± 0.11	0.8 ± 0.3	19 ± 10^a	8.0
WB89-060	-83.99 ± 0.10	1.4 ± 0.3	64 ± 20	10.0
WB89-076	-96.99 ± 0.05	1.7 ± 0.11	104 ± 11	7.0
WB89-080	-74.2	2.9	≤ 39	13.0
WB89-083	-94.00 ± 0.04	0.73 ± 0.09	23 ± 5	7.6
WB89-152	-88.1	0.8	≤ 30	19.5
WB89-283	-94.5	1.2	≤ 11	5.7
WB89-288	-100.9	1.6	≤ 12	8.0

Table A.2. Same as Table A.1 but for $\text{H}^{15}\text{NC}(1-0)$.

Source	v_{LSR} (km s^{-1})	FWHM (km s^{-1})	$\int T_{\text{MB}} dv$ (mK km s^{-1})	σ (mK)
WB89-315	-95.1	2.1	≤ 29	11.0
WB89-379	-89.3	2.2	≤ 13	5.0
WB89-380	-86.7	3.0	≤ 23	8.0
WB89-391	-86.1	1.1	≤ 9	6.0
WB89-399	-82.2	2.2	≤ 33	14.0
WB89-437	-71.7	3.2	≤ 28	7.0
WB89-440	-72.2	1.6	≤ 20	9.0
WB89-501	-58.4	1.3	≤ 14	8.0
WB89-529	-60.1	1.9	≤ 42	11.0
WB89-572	-48.0	0.7	≤ 17	12.0
WB89-621	-25.4	1.8	≤ 13	6.6
WB89-640	-25.4	0.9	≤ 22	16.0
WB89-670	-17.5	0.5	≤ 19	14.0
WB89-705	-12.1	0.9	≤ 20	12.0
WB89-789	34.7	1.4	≤ 20	10.0
WB89-793	30.5	1.7	≤ 41	16.0
WB89-898	63.4	2.3	≤ 30	11.0
19423+2541	-71.3 ± 0.4	2.7 ± 0.9	33 ± 18^a	7.0
19383+2711	-65.7	1.6	≤ 13	6.0
19383+2711-b	-71.2	1.6	≤ 13	6.0
19489+3030	-68.7	1.1	≤ 18	10.5
19571+3113	-62.5	2.3	≤ 22	8.3
20243+3853	-73.1	3.0	≤ 19	6.2
WB89-002	-2.8	1.3	≤ 41	19.0
WB89-006	-90.3 ± 0.3	2.6 ± 0.7	72 ± 31	11.7
WB89-014	-96.0	1.7	≤ 27	12.6
WB89-031	-89.4	1.6	≤ 20	10.0
WB89-035	-77.7	2.2	≤ 20	7.5
WB89-040	-62.5	0.8	≤ 13	8.7
WB89-060	-84.3	1.4	≤ 22	11.0
WB89-076	-97.5 ± 0.3	2.1 ± 0.7	32 ± 19^a	7.11
WB89-080	-74.2	2.9	≤ 39	13.0
WB89-083	-93.8	0.7	≤ 10	7.6
WB89-152	-88.1	0.8	≤ 28	19.5
WB89-283	-94.5	1.2	≤ 12	5.7
WB89-288	-100.9	1.6	≤ 9	8.0

Notes. Parameters without errors are assumed in the fitting procedure, as explained in Sect. 3.2. ^(a) Tentative detection.

Table A.3. Same as Table A.1 but for H¹³CN(1–0).

Source	v_{LSR} (km s ⁻¹)	FWHM (km s ⁻¹)	$\int T_{\text{MB}} dv^a$ (mK km s ⁻¹)	σ (mK)
WB89-315	-95.1	2.1	≤17	12.0
WB89-379	-89.20±0.04	1.68±0.09	102±11	5.0
WB89-380	-86.81±0.14	3.5±0.3	136±23	8.0
WB89-391	-85.98±0.03	1.31±0.07	83±10	6.0
WB89-399	-82.2	2.2	≤20	14.0
WB89-437	-71.65±0.04	2.3±0.1	255±23	7.0
WB89-440	-72.2	1.6	≤12	9.0
WB89-501	-58.37±0.06	0.88±0.14	39±13	8.0
WB89-529	-60.1	1.9	≤21	11.0
WB89-572	-47.41±0.10	0.7±0.3	28±18 ^b	12.4
WB89-621	-25.30±0.03	1.83±0.06	299±20	6.6
WB89-640	-25.10±0.09	0.9±0.2	39±18 ^b	15.0
WB89-670	-17.5	0.5	≤11	14.0
WB89-705	-12.1	0.9	≤10	12.0
WB89-789	34.41±0.08	0.97±0.18	56±21	10.0
WB89-793	30.4	1.7	≤25	16.0
WB89-898	63.1±0.3	2.3±0.6	58±31 ^b	11.0
19423+2541	-72.38±0.09	3.61±0.16	242±24	7.7
19383+2711	-65.85±0.12	2.9±0.3	125±22	6.0
19383+2711-b	-71.20±0.18	2.9±0.4	87±22	6.0
19489+3030	-69.12±0.11	1.7±0.3	58±18	10.5
19571+3113	-62.67±0.11	1.8±0.3	66±20	8.3
20243+3853	-73.30±0.12	2.6±0.3	100±22	6.0
WB89-002	-2.8	1.3	≤21	19.0
WB89-006	-91.6±0.4	2.7±0.7	45±28 ^b	9.9
WB89-014	-96.0	1.7	≤15	12.6
WB89-031	-89.4	1.6	≤11	10.0
WB89-035	-77.86±0.16	2.2±0.4	54±19	7.6
WB89-040	-62.40±0.07	0.99±0.16	43±14	8.7
WB89-060	-84.08±0.04	2.15±0.09	312±29	10.0
WB89-076	-96.87±0.07	1.37±0.17	55±14	7.0
WB89-080	-74.2	2.9	≤22	13.0
WB89-083	-93.8	0.7	≤6	7.6
WB89-152	-88.1	0.8	≤18	19.5
WB89-283	-94.57±0.12	1.2±0.3	18±13 ^b	6.0
WB89-288	-100.9	0.5	≤7	8.0

Table A.4. Same as Table A.1 but for HC¹⁵N(1–0).

Source	v_{LSR} (km s ⁻¹)	FWHM (km s ⁻¹)	$\int T_{\text{MB}} dv$ (mK km s ⁻¹)	σ (mK)
WB89-315	-95.1	2.1	≤31	12.0
WB89-379	-89.34±0.09	1.4±0.2	45±12	5.0
WB89-380	-85.3±0.4	3.5	59±24	7.6
WB89-391	-85.98±0.04	0.9±0.1	30±6	6.0
WB89-399	-82.2	2.2	≤37	14.0
WB89-437	-71.52±0.13	3.0±0.3	133±23	7.0
WB89-440	-72.2	1.6	≤20	9.0
WB89-501	-58.6±0.4	1.7±0.8	32±26 ^a	7.6
WB89-529	-60.1	1.9	≤4	11.0
WB89-572	-48.23±0.07	0.60±0.15	32±15 ^a	12.0
WB89-621	-25.57±0.11	2.4±0.3	96±18	6.6
WB89-640	-25.4	0.9	≤24	16.0
WB89-670	-17.5	0.5	≤17	14.0
WB89-705	-12.1	0.9	≤18	12.0
WB89-789	34.3±0.2	1.2±0.5	35±29 ^a	10.0
WB89-793	30.3	1.7	≤27	16.0
WB89-898	63.4	2.3	≤28	11.0
19423+2541	-72.1±0.4	5±1	81±27	6.4
19383+2711	-65.90±0.14	2.0±0.3	50±14	6.0
19383+2711-b	-71.2	2.9	≤16	6.0
19489+3030	-68.4	1.6	≤21	10.5
19571+3113	-62.29±0.11	1.1±0.3	33±14	8.3
20243+3853	-73.20±0.15	1.6±0.4	32±13	7.0
WB89-002	-2.7	1.3	≤38	19.0
WB89-006	-91.4	2.7	≤33	11.5
WB89-014	-96.0	1.7	≤28	12.6
WB89-031	-89.4	1.6	≤21	10.0
WB89-035	-77.7	2.2	≤18	7.5
WB89-040	-62.5	1.0	≤14	8.7
WB89-060	-84.01±0.08	1.7±0.2	88±17	10.0
WB89-076	-97.18±0.11	1.4±0.3	32±11	7.0
WB89-080	-74.2	2.9	≤37	13.0
WB89-083	-93.8	0.7	≤12	7.6
WB89-152	-88.1	0.8	≤33	19.5
WB89-283	-94.5	1.2	≤13	5.7
WB89-288	-101.16±0.07	0.5	19±12 ^a	8.0

Notes. ^(a) The line integrated intensity of the main hyperfine transition ($F=2-1$) is shown. ^(b) Tentative detection.

Appendix B: Spectra

In this appendix the observed spectra at the rest frequencies of $\text{HN}^{13}\text{C}(1-0)$, $\text{H}^{15}\text{NC}(1-0)$, $\text{H}^{13}\text{CN}(1-0)$, and $\text{HC}^{15}\text{N}(1-0)$ for all the sources are shown. Each spectrum is centred around the velocity, v_0 , obtained from H_2CO observations by Blair et al. (2008). Detected and undetected transitions are indicated with red and blue curves, respectively.

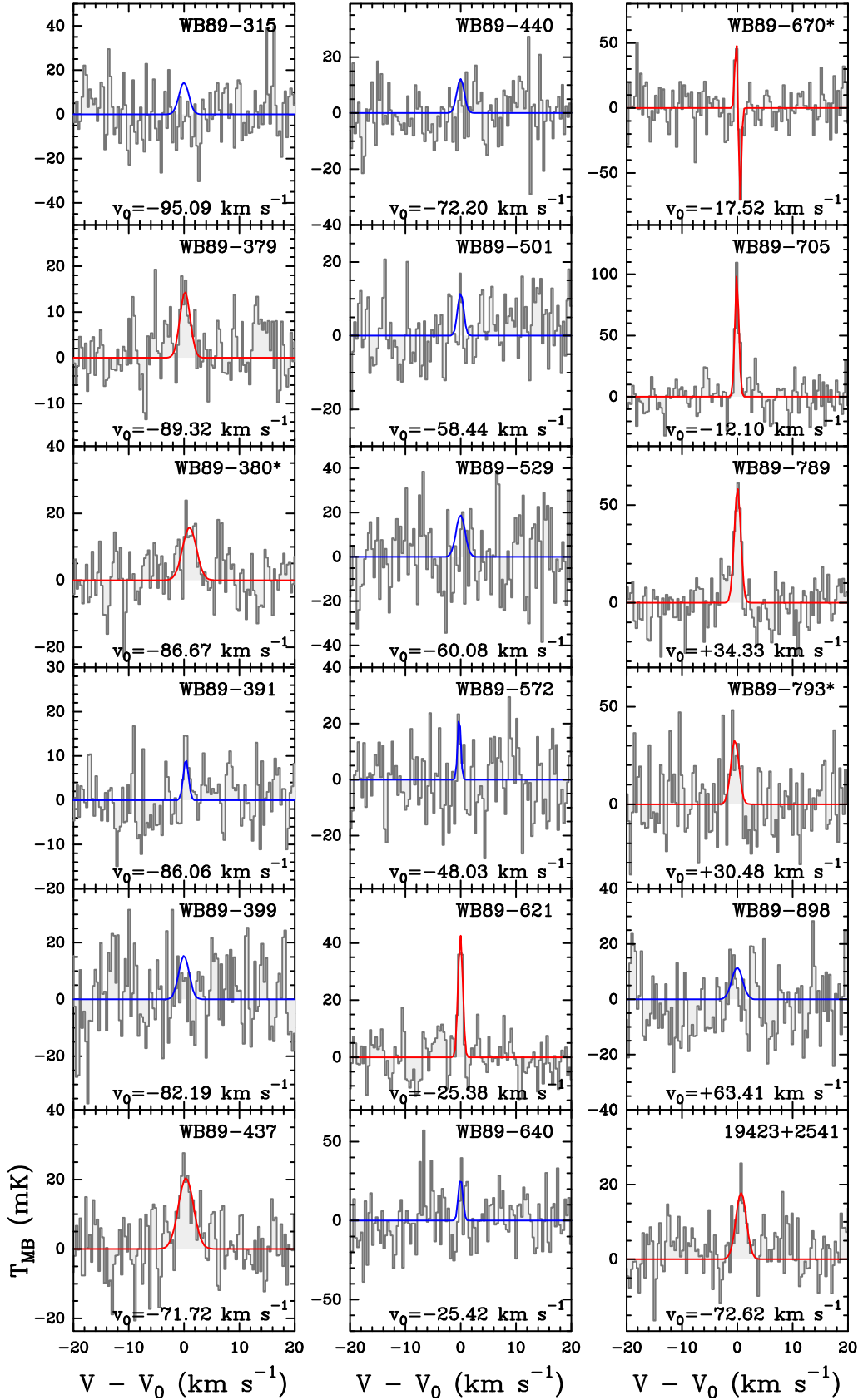


Fig. B.1. Spectra of $\text{HN}^{13}\text{C}(1-0)$ obtained for the sample of sources. For each spectrum the x axis represents a velocity interval of $\pm 20 \text{ km s}^{-1}$ around the velocity, v_0 , obtained from H_2CO observations by Blair et al. (2008). The y axis shows the intensity in main beam temperature units. The red curves are the best LTE fits obtained with MADCUBA for detections and tentative detections (indicated with an asterisk in the source name). The blue curves correspond to the upper limits obtained for non-detections.

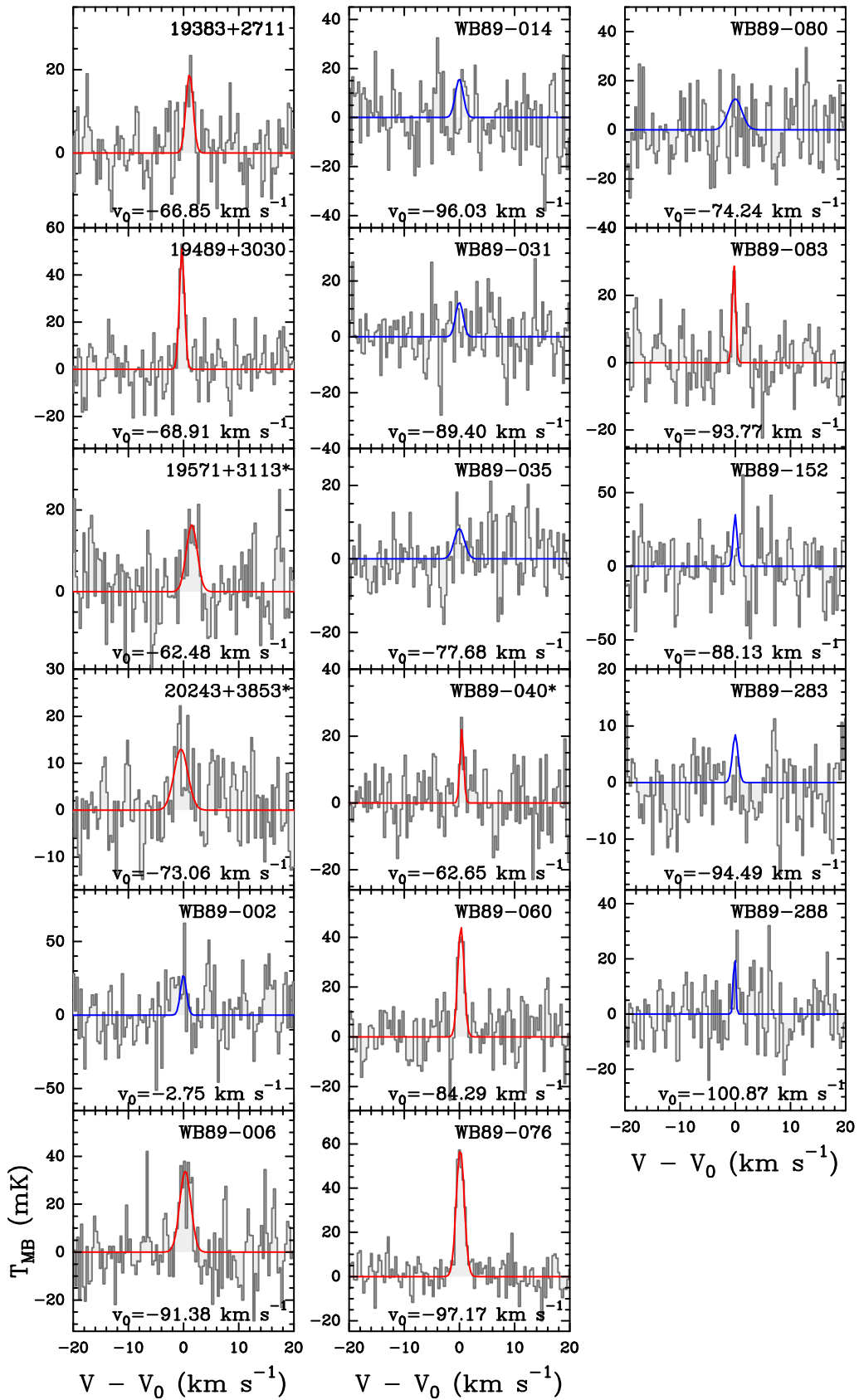


Fig. B.1. Continued.

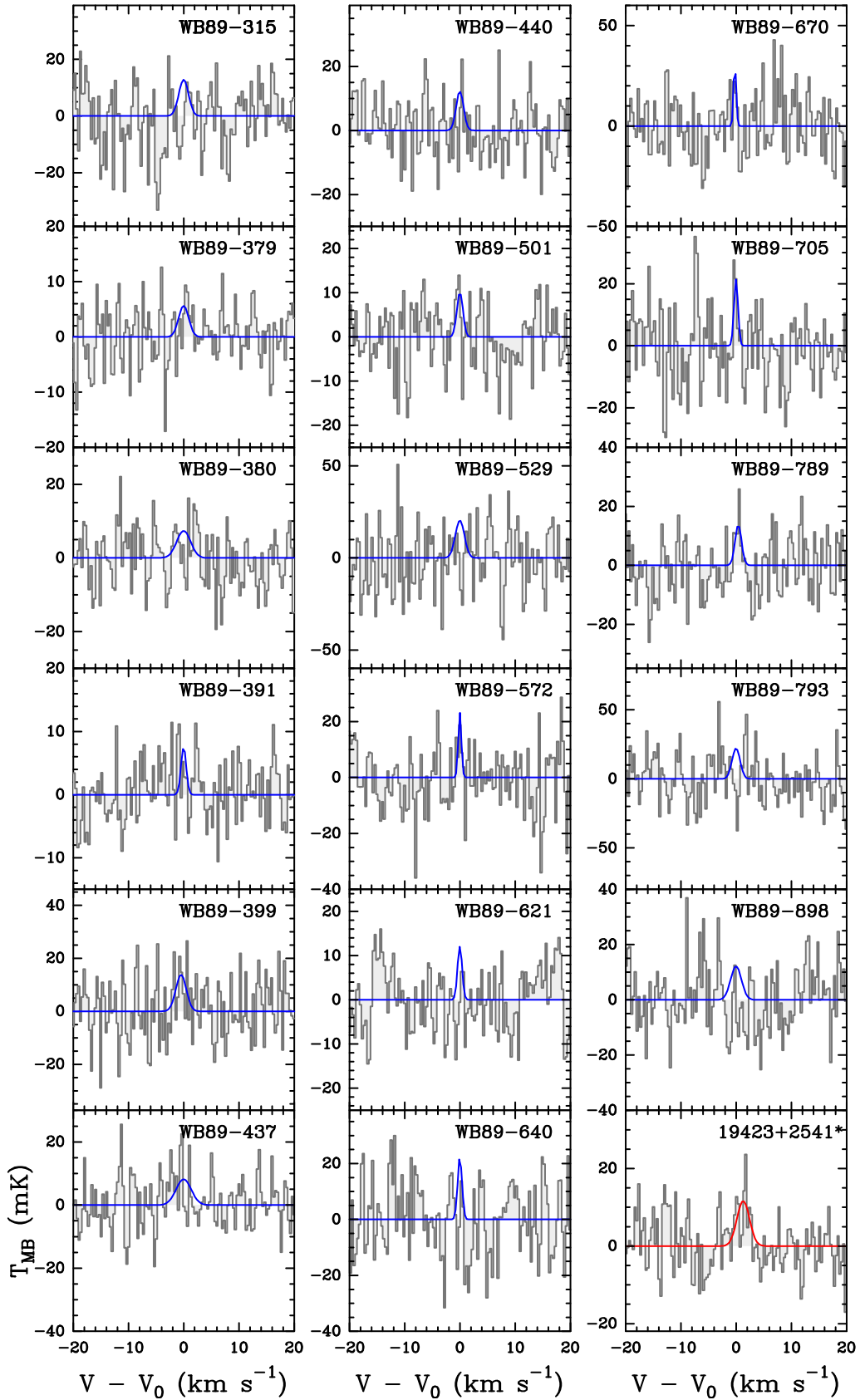


Fig. B.2. Same as Fig. B.1 but for $\text{H}^{15}\text{NC}(1-0)$. The velocity, v_0 , for each source is given in Fig. B.1.

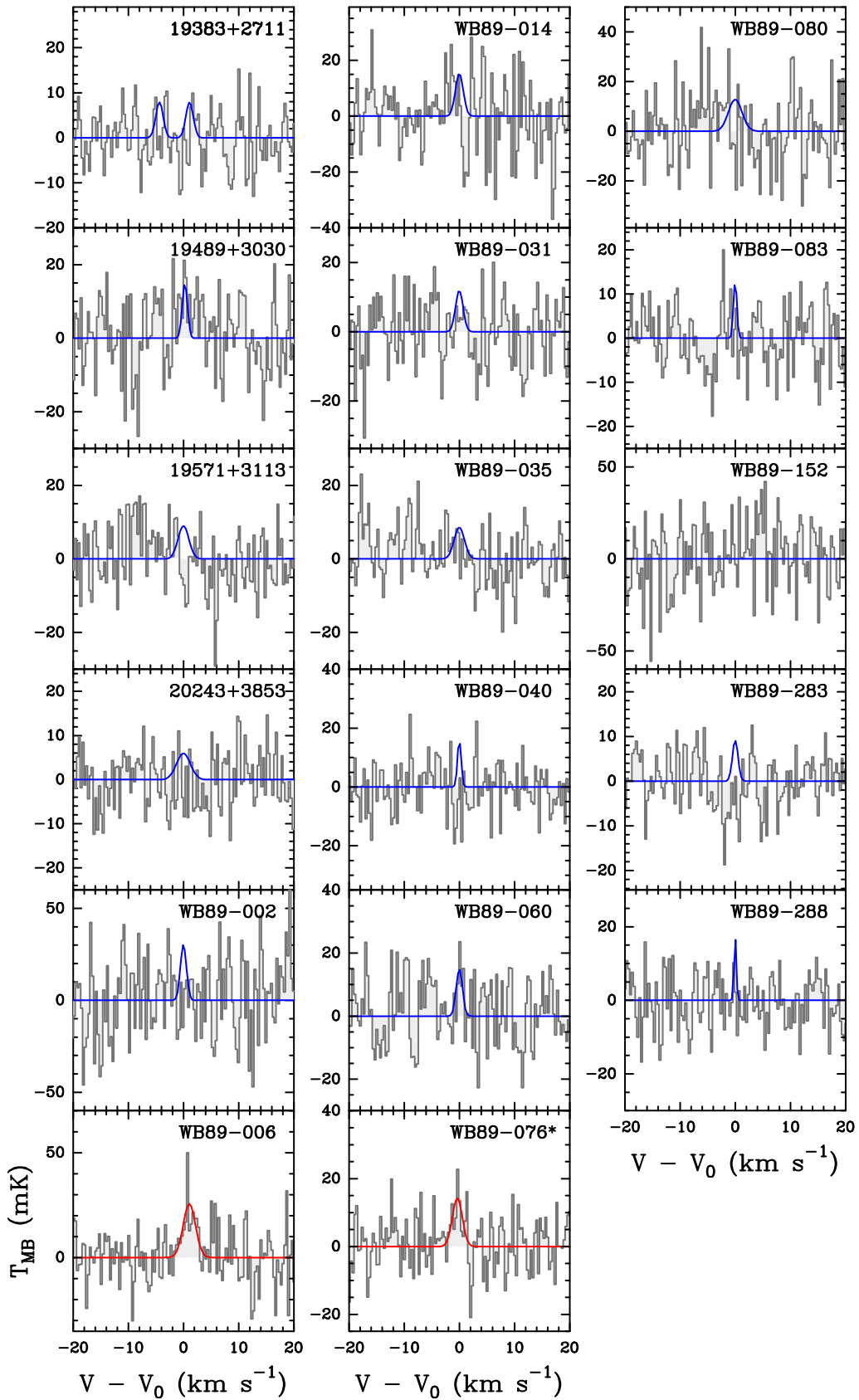


Fig. B.2. Continued.

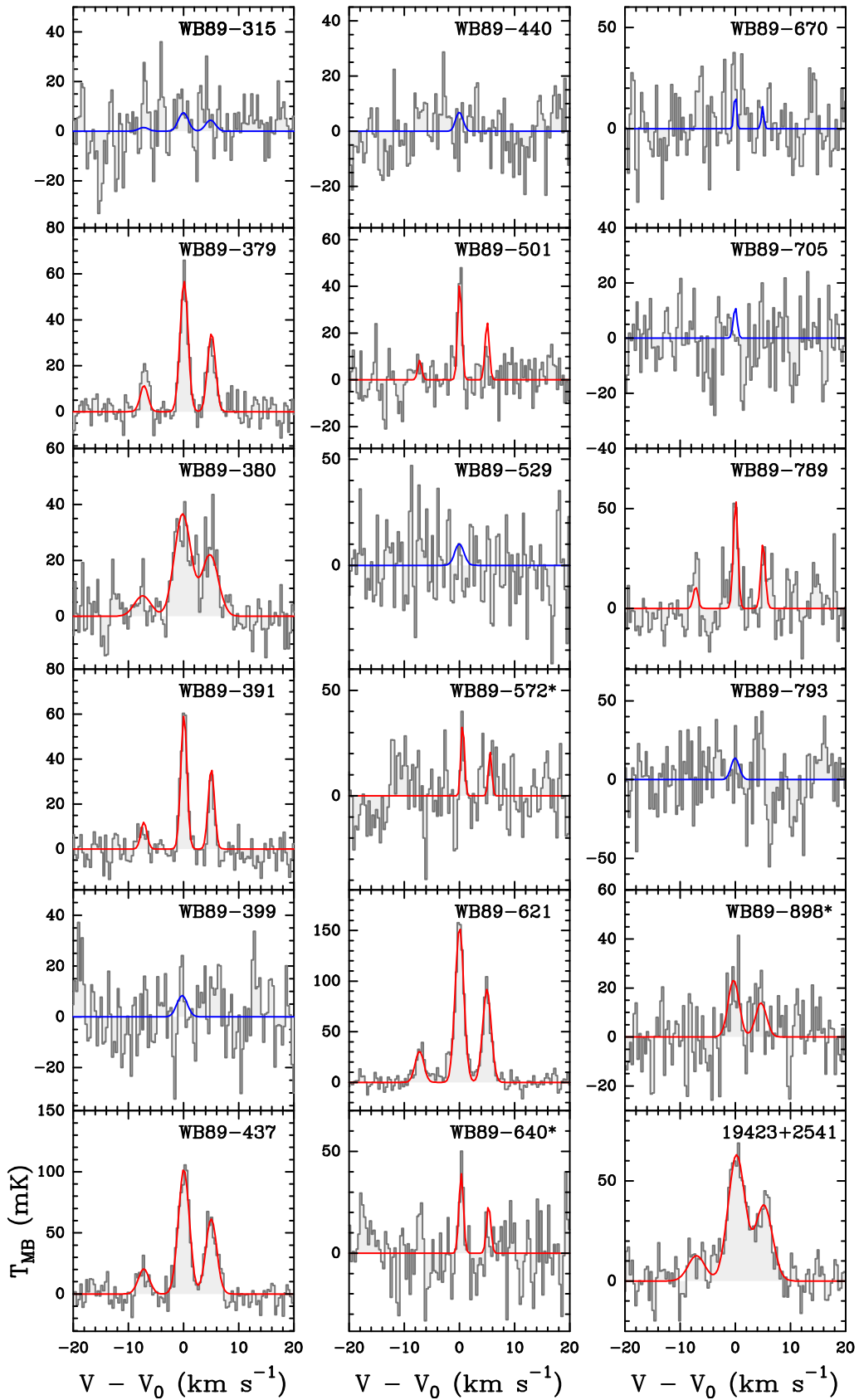


Fig. B.3. Same as Fig. B.1 but for $\text{H}^{13}\text{CN}(1-0)$. The velocity, v_0 , for each source is given in Fig. B.1. For display purposes, only the hyperfine components with LTE peak line intensities above 3σ are shown.

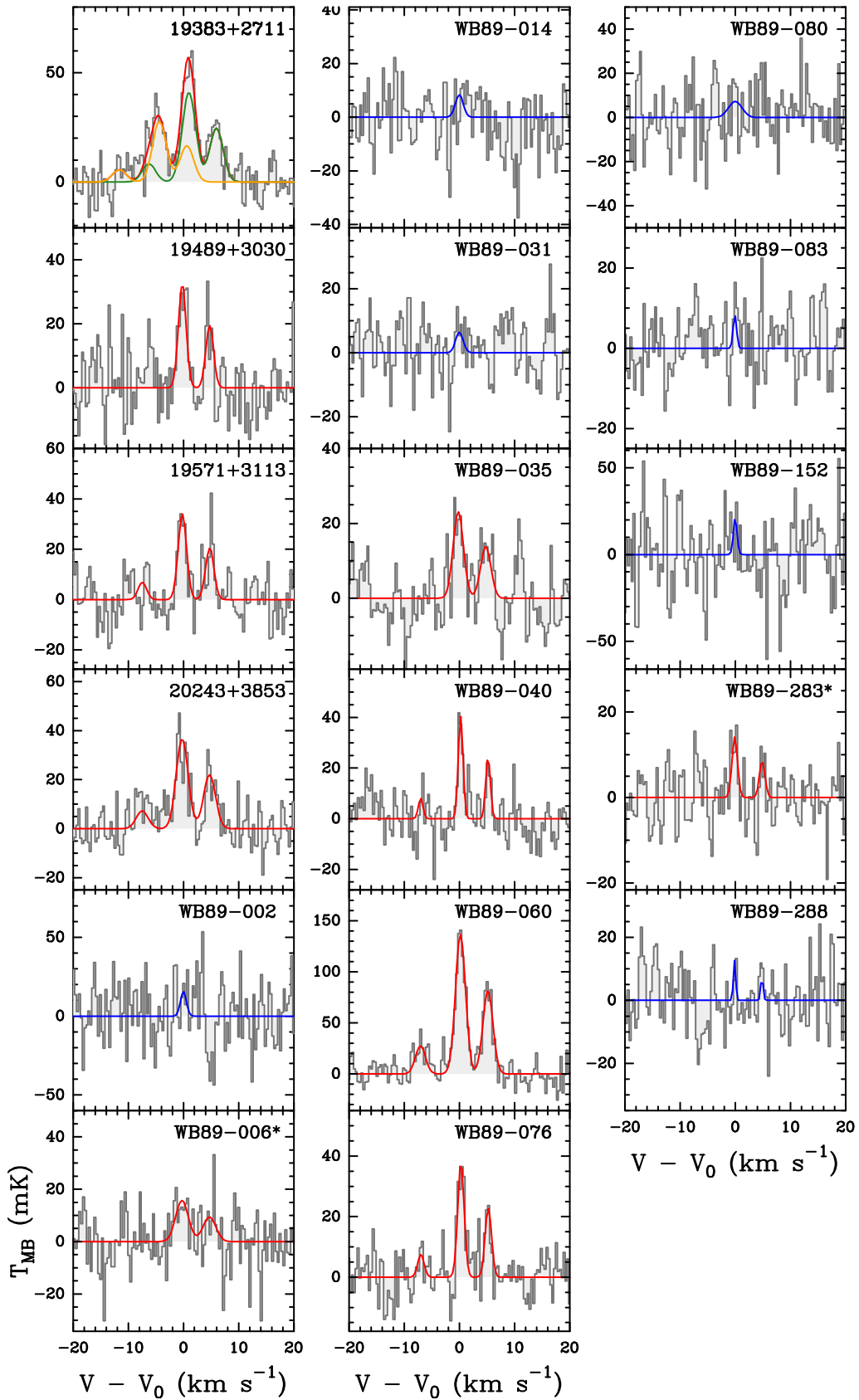


Fig. B.3. Continued. Note that for the source 19383+2711 we have fitted two velocity components (orange curve and green curve). In this case the red curve is the sum of the LTE fit of the two components.

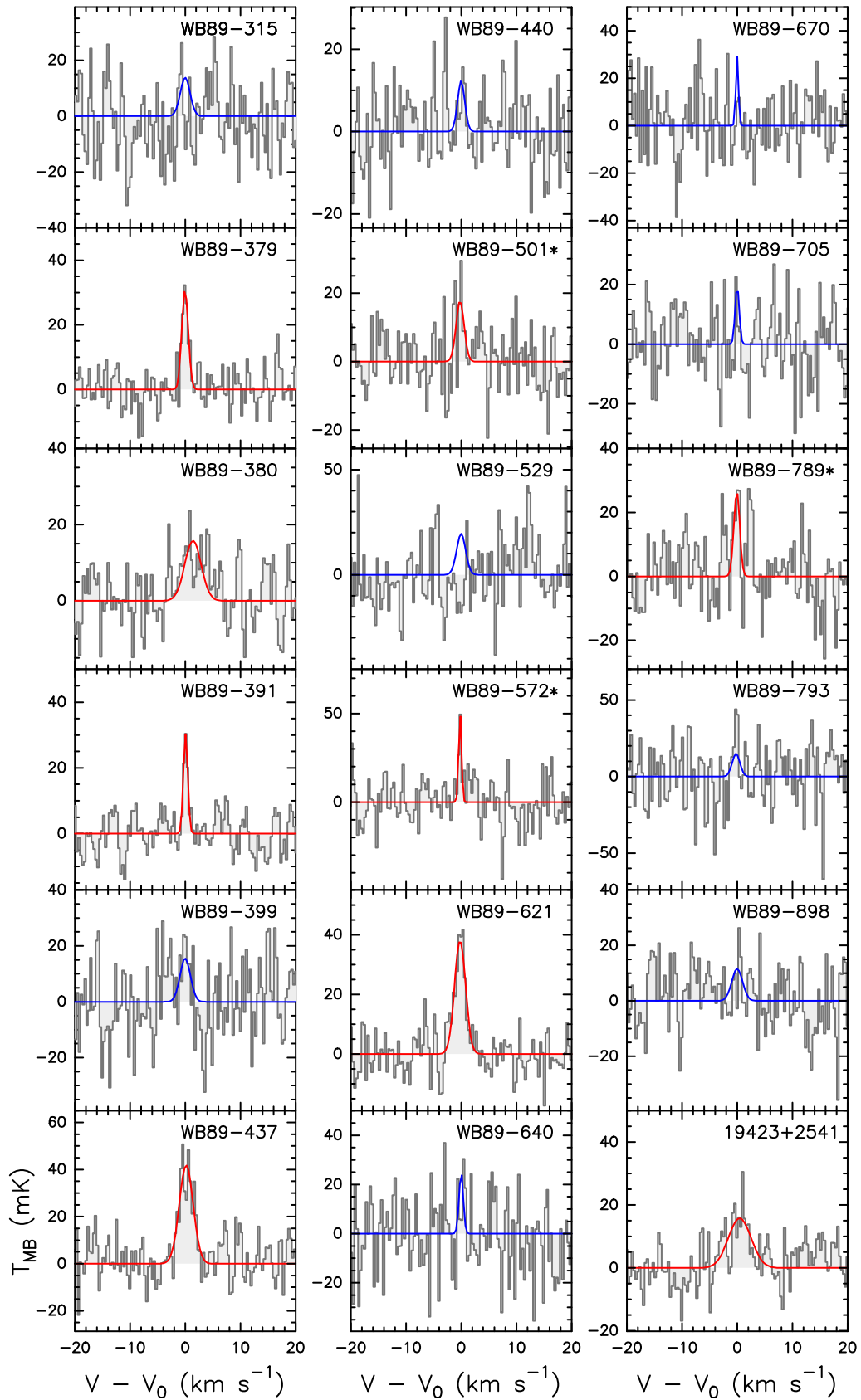


Fig. B.4. Same as Fig. B.1 but for $\text{HC}^{15}\text{N}(1-0)$. The velocity, v_0 , for each source is given in Fig. B.1.

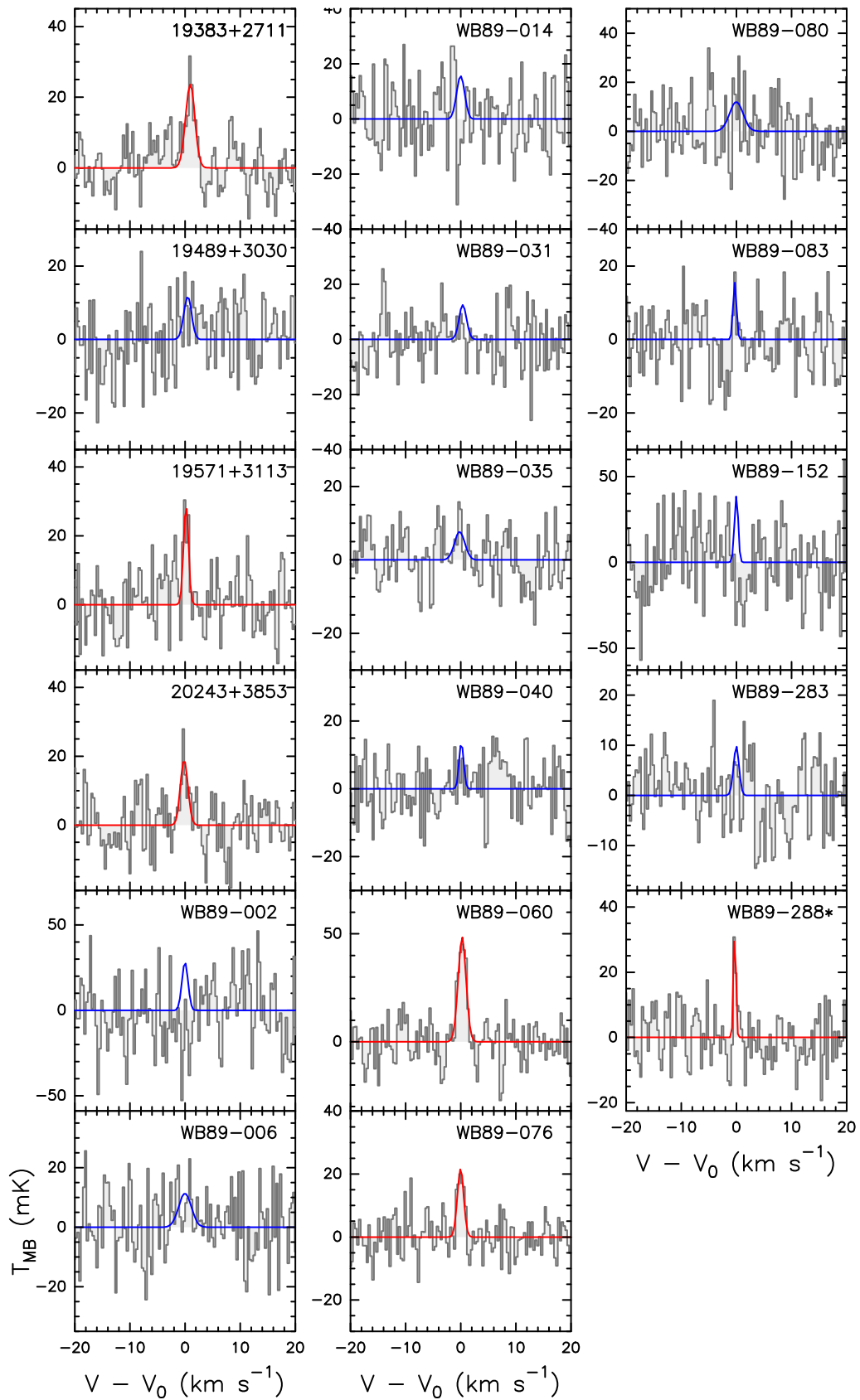


Fig. B.4. Continued.

Appendix C: GCE models: Additional information on the $^{12}\text{C}/^{13}\text{C}$ ratio

In order to convert the $N(\text{H}^{13}\text{CN})/N(\text{HC}^{15}\text{N})$ ratios to isotopic nitrogen ratios, we made use of the $^{12}\text{C}/^{13}\text{C}$ gradient determined by Milam et al. (2005). As mentioned in Sect. 3.3, this trend was obtained for the inner Galaxy, and no observational constraints towards a sample of sources are available so far in the outer Galaxy. In Fig. C.1 we show how the extrapolation of this trend up to $R_{\text{GC}}=20$ kpc compares with the theoretical ratio predicted by the GCE models used in this work. When taking the respective uncertainties into account, a satisfactory agreement is found between observations and theoretical predictions.

We recall that in the GCE model adopted in this work ^{12}C is produced as a primary element in both low- and intermediate-mass stars and massive stars, with the two sources contributing each about half of the solar ^{12}C abundance (Romano et al. 2019). The minor isotope, instead, has both a primary and a secondary origin: a large amount of primary ^{13}C comes from massive fast rotators at low metallicities, while at higher metallicities secondary production in both low- and intermediate-mass stars and massive stars dominates. Our models also include a contribution to ^{13}C synthesis from novae on long timescales.

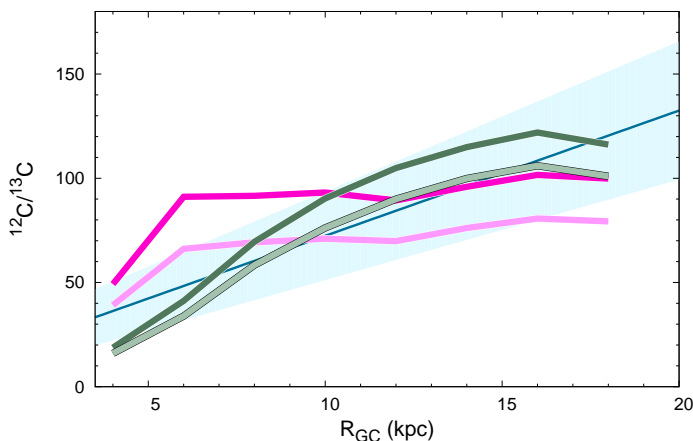


Fig. C.1. Comparison between observed and predicted $^{12}\text{C}/^{13}\text{C}$ ratios. The blue line indicates the observed $^{12}\text{C}/^{13}\text{C}$ ratio trend along the Galactic disc by Milam et al. (2005), with its 1σ uncertainty (light blue shaded area). The observed gradient is compared to the theoretical one obtained from different GCE models (see Table 2).

Appendix D: Azimuthal variations

In this appendix we investigate a dependence with the Galactic longitude. Figure D.1 shows our results in the Galactic plane view of the Milky Way made by Reid et al. (2014). The different colours represent different $^{14}\text{N}/^{15}\text{N}$ ratios, as indicated by the figure labels. As already found in the inner Galaxy by Colzi et al. (2018b), the new sources in the outer Galaxy do not present a clear trend along spiral arms or with the azimuthal angle.

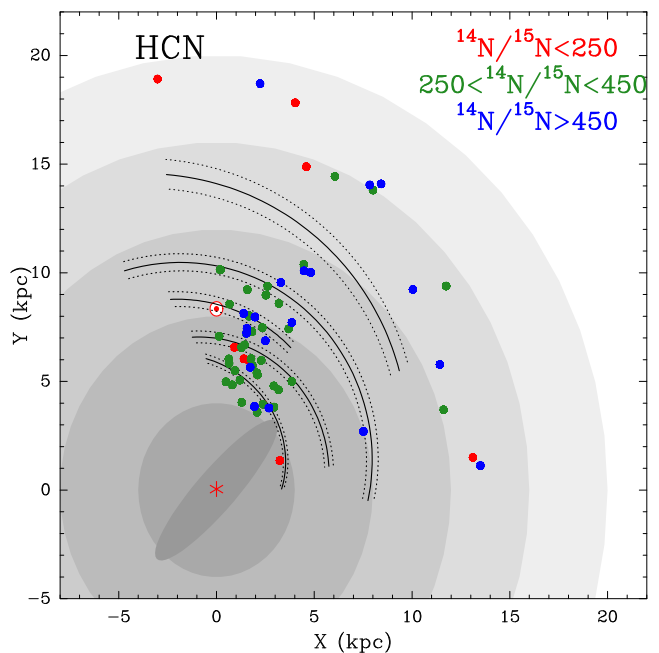


Fig. D.1. Plan view of the Milky Way. The Galactic centre (red asterisk) is at (0,0), and the Sun (red Sun symbol) is at (0,8.34). The background grey discs correspond to the Galactic bar region (~ 4 kpc), the solar circle (~ 8 kpc), co-rotation of spiral pattern (~ 12 kpc), and the edge of major star-formation regions (~ 16 kpc). The solid black lines indicate the centre of spiral arms traced by masers, and the dotted lines the 1σ widths. For more details, see Reid et al. (2014). The filled circles represent the sources studied in this work and in Colzi et al. (2018b), and the three colours are the $^{14}\text{N}/^{15}\text{N}$ ratios measured for HCN: in red values < 250 , in green values in between 250 and 450, and in blue ratios > 450 .